Green Chemistry

PAPER

View Article Online
View Journal

Cite this: DOI: 10.1039/d5gc01277e

Low-energy and green *in situ* recycling of spent lithium-ion batteries to achieve graphite regeneration and pre-lithiation†

Jie Chen,[a] Ruilan Li,[a] Yongzhi Duan,[a] Shuaiqi Gong,*[a] Yulin Min,[a,b] Hexing Li [a,b] and Penghui Shi *[a,b]

The cyclic regeneration of non-renewable graphite anode materials in lithium-ion batteries (LIBs) is crucial for battery recycling, aiming to reduce carbon footprints and minimize resource waste. Traditional methods often involve high energy use and significant environmental pollution. To tackle this, a green, closed-loop regeneration method using only oxalic acid was developed. This approach efficiently recovers precious metals from the anode and allows for *in situ* regeneration of the spent anode, as well as the synthesis of pre-lithiation reagents. The findings indicate that lithium oxalate on the surface of pre-lithiated regenerated graphite compensates for active Li^+ loss and acts as a pre-lithiation sacrificial salt during battery operation. It also decomposes to release carbon dioxide, preventing the formation of soluble lithium alkoxides and electrolyte ester exchange reactions, significantly enhancing battery performance without leaving impurities. This method allows effective lithium utilization from spent anodes and *in situ* closed-loop regeneration. Under optimal conditions, the Li^+ leaching rate reaches 97.64%. The electrochemical performance of the regenerated prelithiated graphite maintains a high specific capacity of 320.5 mAh g^{-1} after 200 cycles, with a specific capacity retention rate of 90.4%. Environmental and economic assessment shows an outstanding economic profit of $3259.22 and a negligible environmental footprint for recycling each ton of retired graphite. This work advances material recycling, reduces the environmental impact of waste batteries, and supports a low-carbon transition.

Received 12th March 2025,
Accepted 30th June 2025

DOI: 10.1039/d5gc01277e

rsc.li/greenchem

Green foundation

1. This study proposes an environmentally friendly and cost-effective *in situ* regeneration method for spent lithium-ion battery anodes, replacing traditional high-energy, high-pollution recycling strategies. Spent graphite anodes can be efficiently recovered by utilizing green oxalic acid in a low-energy process, reducing hazardous waste and preventing resource loss.
2. This method simultaneously enables *in situ* regeneration and pre-lithiation of spent anodes using only oxalic acid. During lithium extraction, the resulting lithium oxalate acts as an effective pre-lithiation reagent, remaining on the regenerated graphite surface to offset lithium-ion loss in the first cycle due to solid electrolyte interphase formation, thereby enhancing electrochemical performance. Moreover, this reagent supplies lithium ions without introducing impurities, instead generating beneficial components in the battery.
3. Future research can build on this functional *in situ* regeneration strategy to optimize procedures and reagents, maximizing the recovery and utilization of spent anodes and their intrinsic resources.

[a]*Shanghai Key Laboratory of Materials Protection and Advanced Materials in Electric Power, Shanghai University of Electric Power, Shanghai 200090, P. R. China. E-mail: sq_gong@shiep.edu.cn, shipenghui@shiep.edu.cn; Tel: +86 18801618059*
[b]*Shanghai Institute of Pollution Control and Ecological Security, Shanghai 200090, P. R. China*

†Electronic supplementary information (ESI) available: Detailed calculation of economic and environmental assessment (Note S1); lithium content in the filtrate following oxalic acid leaching at varying stirring rates (Fig. S1); SEM images of the samples after leaching at rotational speeds of (a) 200 rpm and (b) 400 rpm (Fig. S2); SEM image of C-G (Fig. S3); (a) XRD pattern comparison and (b) Raman spectrum comparison of C-G and R-G (Fig. S4); Li 1s XPS spectra of R-G (Fig. S5); the GITT curve of R-G (Fig. S6); long-cycling performance of the C-G half-cell at 0.2C (Fig. S7); cycling performance and coulombic efficiency of C-G, P-G and R-G full-cells at a 0.2C charge/discharge rate (Fig. S8); cycling performance and coulombic efficiency of the R-G half-cell at a 0.1C charge/discharge rate (Fig. S9); molecular dynamics model of (a) $Li_2C_2O_2$, (b) $LiOCH_3$, (c) Li_2CO_3, (d) $LiOCO_2C_2H_5$, (e) Li_2O, (f) $LiOCO_2CH_3$, (g) LiF, and (h) LiOH (Fig. S10); and electrochemical performance of regenerated graphite using different repair methods (Table S1). (PDF). See DOI: https://doi.org/10.1039/d5gc01277e

1. Introduction

The growing reliance on lithium-ion batteries (LIBs) for portable electronics, electric vehicles (EVs), and energy storage systems has led to a significant increase in the production and disposal of spent batteries. This raises concerns about resource depletion and environmental impact due to the large volume of discarded batteries.[1] While much focus has been placed on recycling cathode materials, the recycling of graphite anodes remains underexplored despite their critical status as a non-renewable resource, which is recognized as a "strategic resource essential for advancing 21st-century high-tech industries".[2–4] With LIBs having a limited lifespan of 3 to 10 years, large quantities of waste batteries, projected to reach 3.7 million tons by 2030, pose significant environmental and economic risks.[5] Efficient recycling of graphite anodes is crucial to reduce pollution, conserve valuable resources, and close the material loop in battery production. Developing effective recycling technologies for anodes will support sustainability, mitigate environmental harm, and promote the circular economy in the battery industry.[6]

The disposal of spent graphite (S-G) from LIB anodes encounters significant challenges, with three primary methods currently employed. Firstly, graphite is often discarded during the crushing and screening process, resulting in substantial resource loss. Secondly, it may undergo energy-intensive high-temperature treatments to improve its graphitization degree. Thirdly, S-G is classified as hazardous waste when mixed with toxic anode materials, including strong acids and alkalis, posing environmental and economic burdens.[7] These methods underscore the urgent need for more sustainable and energy-efficient recycling solutions. The degradation of spent LIB anodes is primarily due to the overgrowth and decomposition of the solid electrolyte interphase (SEI) layer, lithium dendrite formation, and the accumulation of by-products such as dead lithium, although the graphite structure remains largely intact.[8] Current recycling methods typically aim to regenerate graphite by removing impurities or enhancing graphitization,[9] extract valuable metals like lithium through chemical or electrochemical processes,[10–12] or convert graphite into value-added products such as graphene.[13–15] However, these approaches often produce harmful waste, including strong acids or alkalis, and fail to fully utilize the graphite itself.[16,17] S-G anodes, despite containing valuable components like residual lithium carbide and dead lithium, are often overlooked as a resource. Additionally, the SEI layer contributes further lithium in the form of both inorganic and organic compounds such as Li_2CO_3, LiF, Li_2O, and $ROCO_2Li$, which pose significant environmental risks if improperly managed. Studies indicate that lithium concentrations in S-G can exceed environmental safety thresholds, exacerbating disposal and recycling challenges.[18] To address these issues, innovative recycling technologies are critically needed. Such methods should not only recover valuable metals like lithium more efficiently but also maximize the reuse of graphite material. Developing approaches that integrate environmental safety with resource recovery is essential for creating a more sustainable and effective recycling process for spent LIBs.

In LIBs, the energy density relies on Li^+ transfer between the transition metal oxide cathode and the graphite anode.[19] The low initial coulombic efficiency (ICE, typically <90%) results from Li^+ consumption during SEI formation in the initial cycle. The SEI layer, crucial for battery performance, prevents solvent co-intercalation, protects electrodes from electrolyte degradation, and functions as an electronic insulator to prevent internal short circuits. Li^+ for SEI formation comes from the electrolyte and the cathode, leading to irreversible lithium loss and reduced capacity in subsequent cycles.[20–22] Over the past decade, various strategies have aimed to mitigate this lithium loss. Sun *et al.* introduced an anode pre-lithiation additive with nanoscale transition metals and lithium oxide.[23] Similarly, Ji *et al.* employed solvent-assisted ball milling for pre-lithiating silicon anodes.[24] Huang *et al.* improved redox reactions in lithium–sulfur batteries through diaphragm pre-lithiation.[25] Among these, anode pre-lithiation is the most effective in reducing lithium loss due to SEI formation and other side reactions.[26–28] Chemical,[29] electrochemical,[30] and contact pre-lithiation methods[31,32] have been extensively studied. Additionally, pre-lithiation reagents have been used to directly regenerate spent cathode materials. For instance, Fan *et al.* pre-lithiated the diaphragm to compensate for lithium loss in the cathode, thereby regenerating lithium iron phosphate batteries.[33] However, challenges such as the air stability of pre-lithiation reagents and the introduction of new impurities have limited their broader application.[34] We explored repurposing residual lithium from spent LIB anodes for anode pre-lithiation using an eco-friendly, low-energy method, regenerating pre-lithiated anodes. Organic lithium salts, such as lithium oxalate ($Li_2C_2O_4$), show promise as "sacrificial" pre-lithiation additives for LIBs and Li^+ capacitors due to their high theoretical capacity and air stability.[35] During the first charge cycle, these small organic lithium salts decompose, releasing gas that can suppress side reactions or be safely vented without compromising energy density.[36] Additionally, oxalic acid has proven effective for lithium extraction, suggesting feasibility for an *in situ* closed-loop regeneration process.[37] Lithium can be extracted from spent LIB anodes using oxalic acid and converted into a pre-lithiation reagent for reuse, enabling the recycling of spent graphite into pre-lithiated regenerated graphite and providing a sustainable LIB recycling solution.

This study presents a green, closed-loop process for *in situ* recycling of spent LIB anodes, using oxalic acid as the sole reagent. In the leaching stage, spent anodes are treated with an oxalic acid ($H_2C_2O_4$) solution to extract Li^+ and residual lithium, mainly as lithium oxalate, along with some $H_2C_2O_4$ and $HC_2O_4^-$. In the regeneration stage, the solution is heated to concentrate $H_2C_2O_4$, promoting partial decomposition. After heating, the solution is washed with ethanol to remove residual acid, resulting in graphite anodes enriched with lithium oxalate. The mechanism relies on the efficient extraction of lithium *via* the dissociation of oxalic acid under heat,

enhancing the process. The use of a single reagent allows for dual functions: extracting lithium and synthesizing pre-lithiation reagents. This method regenerates the anode with pre-lithiation properties, compensating for lithium loss during battery cycling due to SEI formation. Lithium oxalate decomposes during battery operation, releasing lithium ions and CO_2, boosting performance without leaving solid impurities. As a result, the regenerated anode maintained a higher specific capacity of 320.5 mAh g^{-1} after 200 cycles, with a retention rate of 90.4%. This efficient, low-energy method holds promise for the sustainable, large-scale recycling of spent battery anodes.

2. Results and discussion

2.1 Regeneration process and mechanism of S-G: efficient lithium ion recovery and graphite upgrading and regeneration

S-G from spent LIB anodes contains impurities such as binders, conductive agents, and lithium-containing compounds. Graphite's sp^2 hybridized carbon atoms enable it to store lithium ions during battery operation. As illustrated in Fig. 1a, this study proposes a green and efficient technology for the upgrading and recycling of spent graphite from LIB anodes, consisting of three main steps. First, high-temperature decontamination is performed to remove impurities and obtain P-G. Thermogravimetric analysis (TGA) was conducted to identify the optimal temperature range for impurity removal (Fig. 1b). The TGA curve showed three distinct stages of mass loss. The first stage, starting at around 200 °C, corresponds to the decomposition of residual electrolyte components. The second stage, between 400 °C and 550 °C, involves the thermal decomposition of binders and conductive agents. The third stage, from 550 °C to 800 °C, likely includes the oxidation of graphite. Interestingly, oxidized graphite exhibits increased interlayer spacing and specific surface area, which can enhance its electrochemical properties and provide more defect sites for the attachment of lithium oxalate.[38] To balance impurity removal with the preservation of the graphite structure, a pretreatment temperature of 550 °C was selected.

The high residual lithium content in P-G materials from spent batteries provides a sufficient resource for pre-lithiation

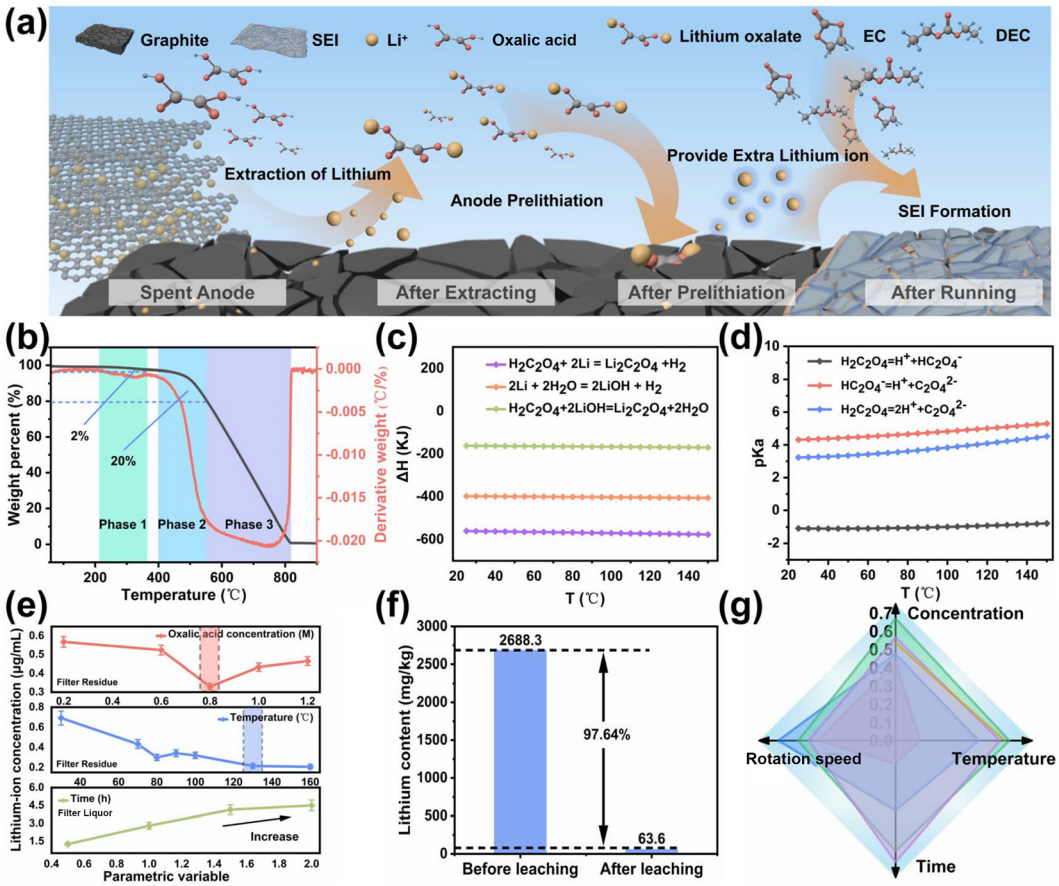

Fig. 1 (a) Schematic illustration of the experimental mechanism; (b) thermogravimetric analysis (TGA) curve of S-G; (c) enthalpy change for the reaction of lithium with oxalic acid and water; (d) dissociation constant of oxalic acid; (e) lithium content in the filtrate at different oxalic acid concentrations and temperatures (red and blue curves), and lithium content in the filtrate at different treatment times (green curve); (f) inductively coupled plasma (ICP) analysis of the P-G material before and after treatment; and (g) radar plot of different leaching conditions.

processes. Therefore, the second procedure in this regeneration process involves extracting lithium from the residual lithium in P-G by adding water and oxalic acid. As shown in Fig. 1c, thermodynamic analysis supports the feasibility of using oxalic acid for lithium extraction. Fig. 1d demonstrated that both deionized water and oxalic acid are effective in extracting lithium. Specifically, lithium carbide, an intercalation compound, easily decomposes upon contact with water, releasing lithium ions. Additionally, lithium metal reacts with water to form lithium hydroxide, which then reacts with oxalic acid to produce lithium oxalate and water. These reactions are thermodynamically favorable, driving the overall process toward the efficient formation of lithium oxalate, ensuring effective lithium extraction during the regeneration process. The optimal conditions were determined using an orthogonal experimental design, considering factors such as oxalic acid concentration, reaction temperature, reaction time, and stirring speed (Fig. 1e and S1, S2†). The results indicated that a 0.8 M oxalic acid concentration, 130 °C temperature, and a stirring speed of 200 rpm provided the most effective lithium extraction. Inductively coupled plasma (ICP) analysis (Fig. 1f) of the P-G material treated with water and oxalic acid revealed a significant reduction in lithium content, from 0.27% (2688.3 mg kg^{-1}) in the untreated P-G to 0.0064% (63.6 mg kg^{-1}) in the processed samples, achieving a lithium leaching efficiency of 97.64%. These conditions were ultimately selected based on the balance of extraction efficiency and energy consumption, ensuring optimal performance while minimizing resource usage (Fig. 1g).

The final step involves the evaporation and concentration of the lithium oxalate solution, which is combined with a suspension of P-G powder, to achieve the upgrading and regeneration of the spent graphite. This process results in the formation of R-G with enriched $Li_2C_2O_4$, completing the recycling procedure. The concentration process ensures the effective deposition of lithium oxalate onto the graphite surface, thereby enhancing its electrochemical performance and restoring its structural integrity for further use in lithium-ion batteries.

2.2 Characterization and analysis of pre-lithiated recycled graphite

The morphology of S-G, P-G, and R-G was analyzed using scanning electron microscopy (SEM) and transmission electron microscopy (TEM). SEM images (Fig. 2a–c) revealed that S-G had a surface heavily contaminated with impurities and lithium dendrites. In contrast, the surface of pretreated P-G showed significant impurity reduction and the formation of pores, likely due to the removal of impurities and partial graphite decomposition at high temperatures. The formation

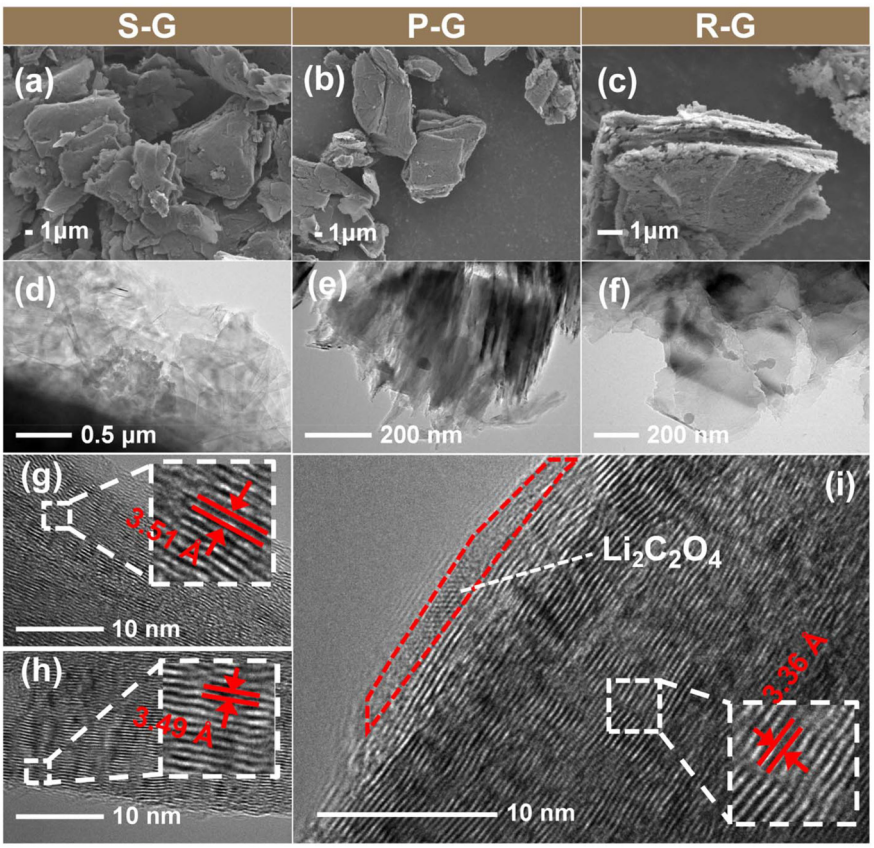

Fig. 2 SEM images of S-G (a), P-G (b), and R-G (c); TEM images of S-G (d), P-G (e), and R-G (f); and HRTEM images of S-G (g), P-G (h) and R-G (i).

of these pores is beneficial for ion transport and electrolyte penetration, enhancing lithium-ion migration during battery operation. Moreover, the increased surface area provides sites for lithium oxalate attachment, positively influencing ion storage and diffusion.[39] Fig. 2c shows that R-G exhibits a layer of lithium oxalate on its surface while retaining a superior lamellar structure, similar to that of commercial graphite (C-G, Fig. S3†). Although the surface of R-G is slightly rougher than C-G, the pores on the surface increase lithium storage at the graphite edges, improving lithium diffusion efficiency.[40] TEM analysis (Fig. 2d–f) further supports these observations, showing agglomerated impurities in S-G, dead lithium and lithium carbide in P-G, and a larger number of particles, likely lithium oxalate, on the surface and interlayers of R-G. These particles confirm the successful formation of lithium oxalate during the regeneration process. Lattice spacing analysis through high-resolution TEM (HRTEM) images (Fig. 2g–i) provided further insights into the structural changes. The lattice spacing for S-G and P-G was 3.51 Å and 3.49 Å, respectively, which is larger than the standard value of 3.36 Å for the (002) plane in graphite due to the presence of impurities such as electrolyte, binder, and lithium compounds. In contrast, the lattice spacing of R-G was 3.36 Å, consistent with the standard (002) plane, indicating that the regeneration process restored the graphite structure. Notably, in the region highlighted by the red box, the lattice stripes on the surface of R-G differ from those inside, further confirming the presence of lithium oxalate on the surface, which enhances the material's structural integrity, ion storage capacity, and diffusion efficiency.

To investigate the chemical changes during the recycling and prelithiation process, X-ray diffraction (XRD), Raman spectroscopy and infrared (IR) spectroscopy were performed on S-G, P-G, and R-G. The XRD patterns shown in Fig. 3a reveal that the graphite crystal structure remains stable across all samples, as evidenced by the consistent reflection of the (002) peak. However, variations in the d (002) spacing were observed with R-G showing the largest d (002) spacing (Fig. 3b). This suggests that R-G possesses a more favorable lamellar structure orientation, enhancing ion intercalation and deintercalation capabilities compared to S-G and P-G. The orientation index (OI), calculated as the ratio of the (002) to (100) peak intensity, further confirms this. R-G exhibited the highest OI value of 246, compared to 98 for S-G and 225 for P-G, indicating improved electrolyte infiltration and high-rate performance. Additionally, when compared to commercial graphite (C-G) (Fig. S4a†), R-G demonstrated superior structural properties. Raman spectroscopy (Fig. 3c) shows that the I_D/I_G ratio, which reflects the degree of graphitization, decreased

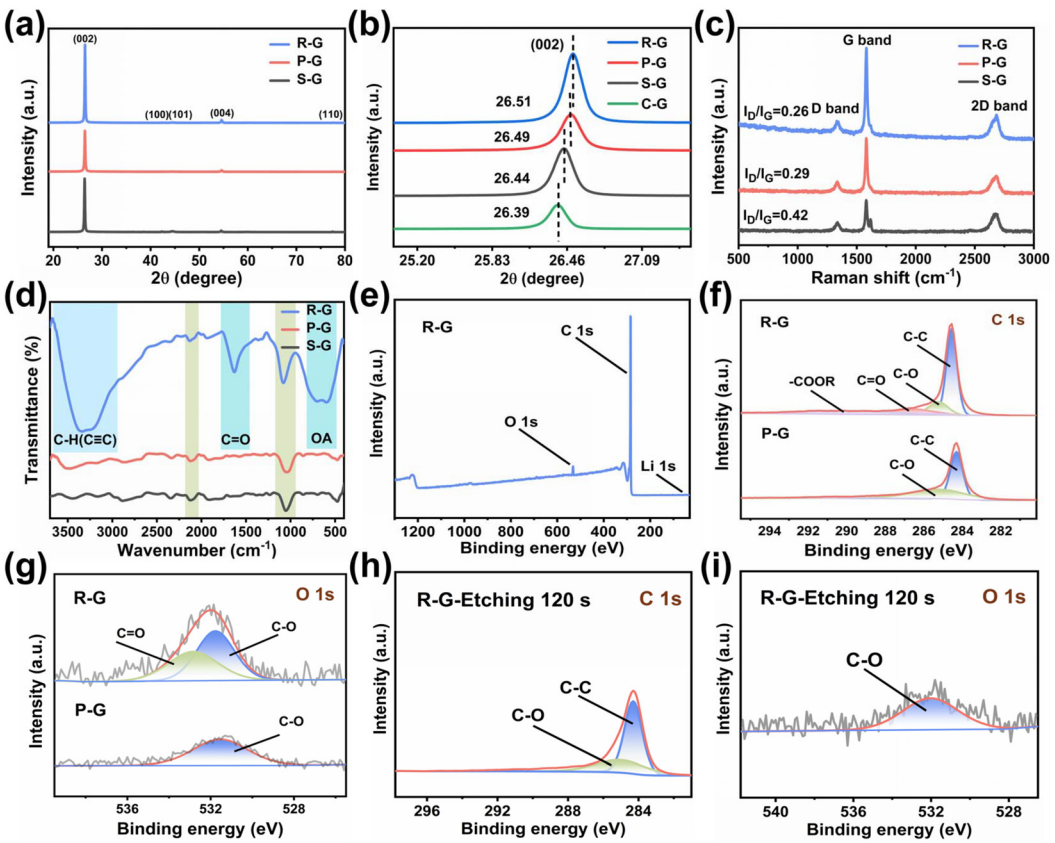

Fig. 3 (a) XRD patterns of S-G, P-G, and R-G; (b) amplified XRD peaks on the (002) plane; (c) Raman spectra and (d) IR spectra of S-G, P-G, and R-G; (e) full XPS spectra, (f) C 1s XPS spectra and (g) O 1s XPS spectra of P-G and R-G; (h) C 1s XPS spectra and (i) O 1s XPS spectra of the R-G surface after etching for 120 s.

from 0.29 for P-G to 0.26 for R-G. This indicates that the regeneration process, facilitated by lithium removal through oxalic acid treatment, reduces defects and enhances graphitization.[41] In contrast, S-G had an I_D/I_G ratio of 0.42, consistent with its lower graphitization. The decrease in defects in R-G, along with the intensity increase in the G peak, further confirms the superior structural integrity of R-G compared to P-G. Fig. S4b† shows an I_D/I_G value of 0.36 for C-G, aligning with the observed trend. IR spectroscopy (Fig. 3d) revealed the presence of lithium oxalate in R-G, characterized by strong absorption peaks at 764 and 1642 cm^{-1}. These peaks correspond to the C═O bonds in lithium oxalate, confirming its formation during the regeneration process.[42] Additionally, a peak in the 3000–3300 cm^{-1} range, associated with C–H stretching vibrations, indicates the presence of lithium carbide, in which H^+ from oxalic acid likely occupies the sites of Li^+, forming C–H bonds on unsaturated carbons.

X-ray photoelectron spectroscopy (XPS) further confirmed the formation of lithium oxalate and revealed its location. The survey XPS of R-G (Fig. 3e) showed the expected elemental distribution of Li, C and O. In the C 1s core level XPS of R-G (Fig. 3f), four distinct peaks at 284.3 eV, 285.0 eV, 285.8 eV, and 290.0 eV were assigned to C–C bonds, C–O bonds, C═O bonds and –COOR bonds, respectively, indicating the presence of lithium oxalate. In contrast, C 1s XPS spectra of P-G only showed C–C and C–O bonds, further confirming the direct formation of lithium oxalate on R-G. The C═O bonds play a crucial role in energy storage by providing numerous coupled electrons, which enhance rapid redox reactions. Additionally, the peaks in the O 1s XPS spectra at 531.5 and 532.5 eV were associated with C–O and C═O bonds (Fig. 3g). Li 1s XPS spectra are provided in Fig. S5.† To explore the location of lithium oxalate, XPS analysis was conducted on the surface of R-G after etching to a depth of 120 s. As shown in Fig. 3h, the etched surface of R-G only displayed C–C and C–O bonds, with no C═O and –COOR bonds in C 1s XPS spectra, indicating that lithium oxalate is located on the surface. Similarly, in the O 1s spectra (Fig. 3i), only the characteristic peak of the C–O bond at 531.72 eV was detected after etching, further confirming the surface localization of lithium oxalate. This surface-specific formation aligns with the electrochemical improvements observed in R-G.

2.3 Evaluation of electrochemical properties of pre-lithiated recycled graphite

R-G refers to the recycled graphite anode that has undergone pre-lithiation, a process aimed at enhancing its electrochemical properties. To demonstrate the effect of pre-lithiation in this work, a comprehensive set of electrochemical tests was performed. During typical battery operation, lithium ions move from the positive electrode to the negative electrode during charging, where they are intercalated into the graphite structure. Upon discharge, these lithium ions deintercalate and return to the positive electrode. However, in pre-lithiated graphite, lithium ions are already present in the anode material, which results in a greater number of lithium ions being released during the first discharge cycle than the amount initially intercalated. As shown in Fig. 4a, the charge and discharge efficiency, defined as the ratio of Li^+ released to those intercalated, reached an impressive value of 172.46% during the first cycle. This high efficiency, despite a relatively low charging capacity, indicates that the pre-lithiated graphite contains a certain amount of lithium ions, which significantly enhances the battery's capacity during operation. In the second cycle, the efficiency remains greater than 100%, further confirming the positive effect of pre-lithiation on battery performance.

It is well-established that during the first cycle, a portion of Li^+ is consumed in forming the solid electrolyte interphase (SEI) layer, which protects the graphite anode from electrolyte corrosion and enhances lithium-ion transmission efficiency. This process leads to irreversible capacity loss. In Fig. 4b and c, the first charge/discharge capacities for R-G and P-G are compared. The P-G exhibits a first charge capacity of 3.413 mAh and a discharge capacity of 3.280 mAh, resulting in an irreversible capacity loss of 0.133 mAh. In contrast, R-G shows a significantly reduced irreversible capacity of only 0.006 mAh. This reduction can be attributed to the pre-lithiation process, which lowers the loss of lithium ions and, consequently, minimizes the irreversible capacity, demonstrating the effectiveness of pre-lithiation in enhancing the electrochemical stability of the recycled graphite anode. Furthermore, these results further confirm the success of pre-lithiation in the graphite negative electrode.

To further assess the electrochemical performance of R-G, cyclic voltammetry (C-V) measurements were conducted on the half-cell. Fig. 4d displays the curve of an R-G half-cell, with clear redox peaks observed at around 0.1 V and 0.4 V, indicating typical lithium intercalation and deintercalation behavior. Additionally, a reduction peak is observed at the positive electrode during the first cycle, corresponding to the formation of the SEI layer on the graphite. These observations provide further evidence of the successful pre-lithiation process and the stable electrochemical behavior of R-G.

The cycling performance of R-G, compared with S-G and C-G, was evaluated at various current densities, as shown in Fig. 4e. It is evident that S-G exhibits slightly poorer electrochemical performance than both R-G and C-G in terms of both initial specific capacity and performance at high current densities. R-G outperforms C-G at higher current densities, which is attributed to its enhanced Li^+ availability. At high discharge currents, Li^+ must traverse the SEI layer rapidly, which can cause structural damage to the membrane, leading to the detachment of the old SEI layer and initiating a repair process that consumes additional Li^+. However, R-G, with this pre-lithiated Li^+ reserve, effectively mitigates this loss, resulting in better performance under high-current cycling. The specific capacities of both C-G and R-G stabilize when the current density is reduced back to 0.2C, indicating that no irreversible reactions have occurred and electrodes retain their structural integrity.

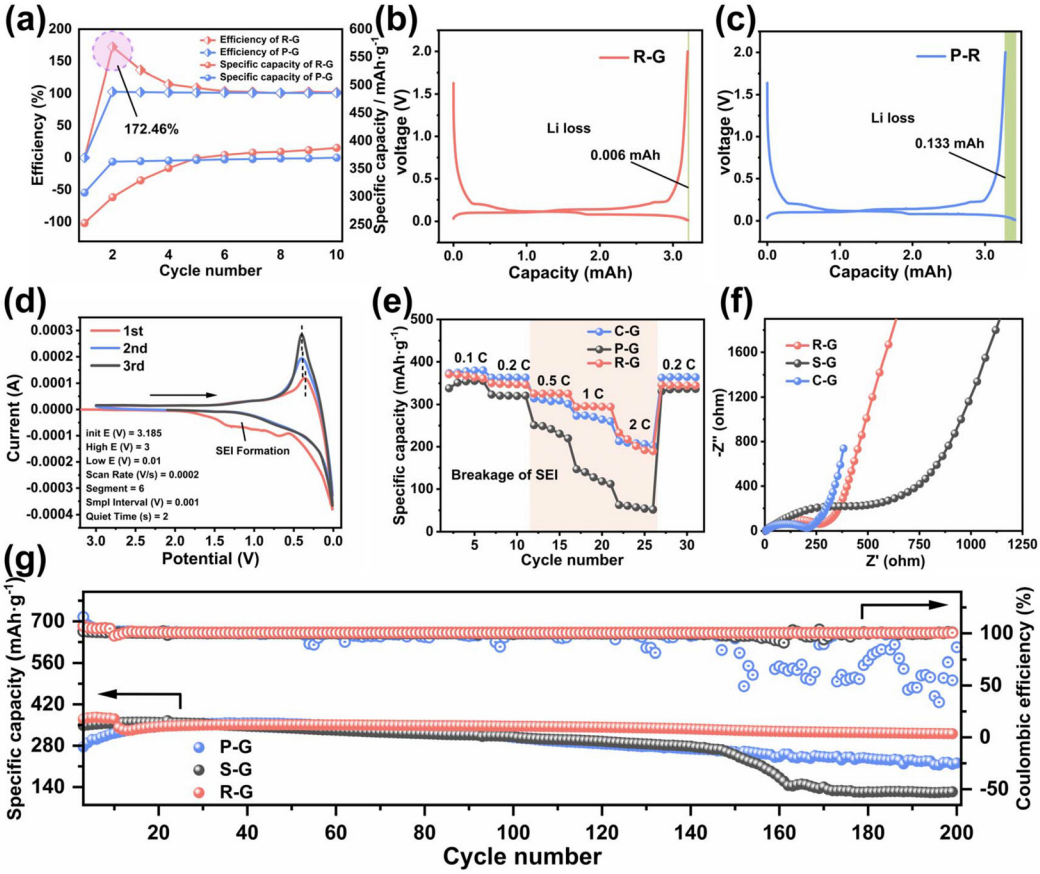

Fig. 4 (a) Charge–discharge efficiency *versus* charge capacity for R-G; the initial charge–discharge profile of (b) R-G and (c) P-G; (d) C–V curves of the first three cycles for R-G; (e) specific capacity of S-G, R-G and C-G at different charge–discharge rates (0.1C, 0.2C, 0.5C, 1C, 2C, and 0.2C); (f) impedance spectra of S-G, R-G, and C-G; and (g) cycling performance and coulombic efficiency of P-G, S-G and R-G half-cells at a 0.2C charge/discharge rate.

Electrochemical impedance spectroscopy (EIS) was also performed to evaluate the charge transfer resistance of the different materials. Fig. 4f shows the impedance plots of S-G, C-G, and R-G, where the semicircle diameter represents the impedance of the electrochemical reaction. A smaller diameter indicates lower impedance and faster electrochemical reaction kinetics. R-G exhibits a semicircle diameter between those of S-G and C-G, with a value closer to that of commercial graphite, suggesting enhanced conductivity and faster charge transfer characteristics. Moreover, the slope of the low-frequency straight line, which represents the charge transfer resistance, is steeper for R-G than for S-G, comparable to C-G, further confirming that pre-lithiation improves the charge transfer properties of the recycled graphite anode. To further evaluate the lithium storage mechanism of interlayer lithium storage, the Li^+ diffusion coefficients of R-G are performed using the galvanostatic intermittent titration technique (GITT). As shown in Fig. S6,† the Li^+ diffusion coefficients of R-G fluctuate between 10^{-10} and 10^{-14} cm^2 S^{-1} at different voltages, indicating the fast Li^+ diffusion rate.

Long-cycling stability tests were performed at a current density of 0.2C to evaluate the longevity of R-G. As shown in Fig. 4g, R-G initially exhibits higher capacity and efficiency compared to S-G, which can be attributed to the pre-lithiation process. After 140 cycles, the specific capacity of S-G drops significantly and stabilizes around 100 mAh g^{-1}. In contrast, R-G maintains a higher specific capacity of 320.5 mAh g^{-1} even after 200 cycles, with an impressive capacity retention rate of 90.4% and only 9.6% capacity loss. Notably, the lithium-storage capability of R-G in this work is more attractive compared to other methods (Table S1†). The long-cycling performance of the C-G half-cell at 0.2C is not unsatisfactory (Fig. S7†). Meanwhile, the cycling performances and coulombic efficiencies of C-G, P-G and R-G full-cells at a 0.2C charge/discharge rate have the same trend, showing a comparable performance of R-G to that of C-G (Fig. S8†). To ensure the reliability of recycled graphite, extended cycling tests are performed at 0.1C, showing that the specific capacity retention remains above 70% after 800 cycles (Fig. S9†). This outstanding cycling stability highlights the advantages of pre-lithiation in enhancing the long-term electrochemical performance of recycled graphite anodes. Notably, compared to other works, R-G in this work exhibits an attractive lithium-storage capability of 320.5 mAh g^{-1}.

2.4 Mechanism of regeneration and pre-lithiation process for a spent graphite anode recycled with lithium oxalate

Graphite, composed of sp^2 hybridized carbon atoms, offers a relatively simple structure compared to cathode materials, which aids in its regeneration. Each carbon atom in the graphite lattice forms three σ-bonds with neighboring carbon atoms, while the remaining p-orbital of each carbon atom participates in π-bonding. This configuration creates a highly conductive material with a specific site for Li^+ storage during the LIB's charge and discharge cycles. During these cycles, lithium ions are continuously intercalated and deintercalated at the negative electrode, with a fraction of lithium remaining trapped within the graphite. This residual lithium may exist in the form of lithium dendrites or intercalation compounds, and a portion of it also resides within the broken SEI layer that remains on the graphite surface after usage.

To recover and utilize this residual lithium, a pre-lithiation process is employed, involving the decomposition of $Li_2C_2O_4$. Lithium dendrites and intercalation compounds can react with water and acids to form lithium hydroxide or lithium oxalate, which is thermodynamically favorable. Oxalic acid, despite being weak, can promote this reaction, especially under heating conditions that enhance the leaching efficiency of Li. The process begins with the removal of water from graphite *via* evaporation and concentration, leaving behind three solid phases: oxalic acid, lithium oxalate, and graphite. Given that $Li_2C_2O_4$ is insoluble in ethanol and oxalic acid is soluble, a simple ethanol rinse can remove excess oxalic acid, leaving pre-lithiated graphite with a $Li_2C_2O_4$ coating.

The advantage of employing $Li_2C_2O_4$ in this pre-lithiation process stems from its high specific capacity, cost-effectiveness, and the fact that it decomposes cleanly without leaving residues, unlike other commonly used pre-lithiation reagents such as Li_3N, Li_3P, Li_2S, and Li_2O_2, or lithium-rich transition metal oxides (*e.g.*, Li_2MoO_3), which often suffer from poor air stability and leave solid residues, diminishing battery energy density. $Li_2C_2O_4$, soluble in water but not in alcohols and ethers, dissolves in the electrolyte, engaging in a solvation-controlled mechanism during the pre-lithiation process. Theoretical calculations of ionic conductivities, shown in Fig. 5a and S10,† reveal the solubility of various lithium salts in the electrolyte, following the order: $LiOCO_2CH_3$ > LiOH > $LiOCO_2C_2H_5$ > $LiOCH_3$ > LiF > $Li_2C_2O_4$ > Li_2CO_3 > Li_2O. This solubility is crucial for the pre-lithiation mechanism, enabling the dissociation of $Li_2C_2O_4$ into Li^+ during battery cycling.[43]

When $Li_2C_2O_4$ is applied to recycled graphite surfaces, it initially adheres to the surface. The use of a water-based binder and deionized water as a solvent during the battery assembly process facilitates the uniform distribution of $Li_2C_2O_4$ on the graphite surface. During battery operation, $Li_2C_2O_4$ decomposes in a voltage range of 4.16 V to 4.70 V in the first cycle, releasing CO_2 and Li^+.[44] The free Li^+ generated during this process contributes to the formation of the SEI layer while playing a vital role in enhancing the long-term stability and performance of the battery. The remaining $Li_2C_2O_4$ decomposes into CO_2, which contributes to the formation of an organic/inorganic SEI layer. It can't be denied that various side reactions occur during battery cycling, including the production of gases. These reactions can be influenced by factors such as electrolyte oxidation by oxygen or electron interactions.[45] However, the existence of CO_2 helps inhibit the formation of soluble lithium alkane oxides (LiOR) and the subsequent electrolyte transesterification reactions.[46]

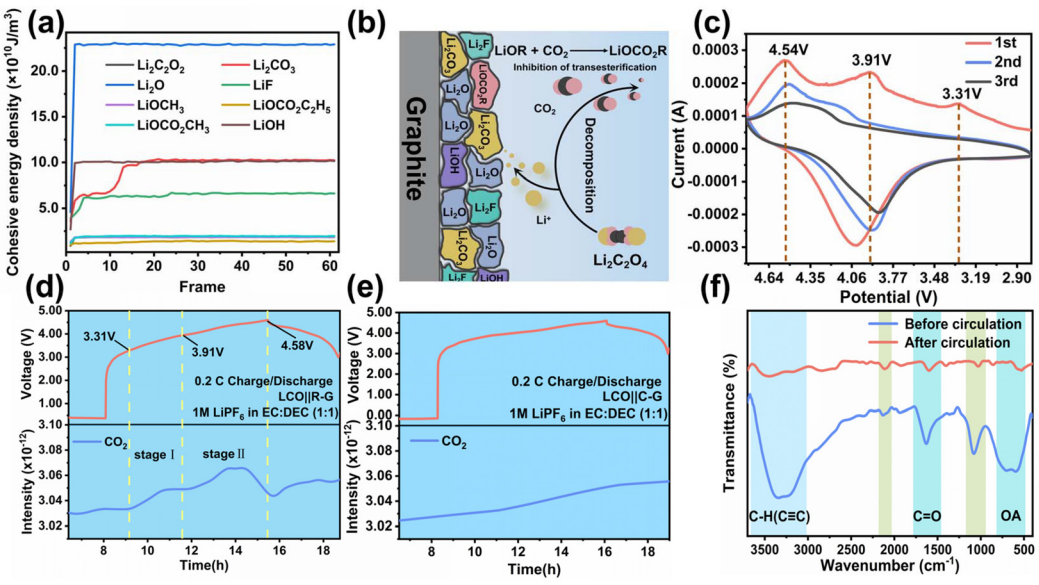

Fig. 5 (a) Molecular dynamics (MD) calculations of the solubility of different substances in the electrolyte; (b) diagram of the decomposition mechanism of $Li_2C_2O_2$ during battery operation; (c) C–V curves of the first three cycles for R-G full cells; differential electrochemical mass spectrometry of C-G (d) and R-G (e) full cells, respectively; and (f) infrared (IR) spectra of the samples before and after the battery cycle.

Furthermore, CO_2 acts as a scavenger for detrimental trace water and protons and can form Li_2CO_3, thus contributing to the formation of an organic/inorganic SEI layer.[47] This SEI layer provides structural integrity and helps suppress the growth of lithium dendrites. Thus, the pre-lithiation reagent used in this experiment not only supplies Li^+ during its operation but also leaves behind substances that positively impact battery performance, rather than remaining as impurities (Fig. 5b). The relative reactions are shown below:

$$Li_2C_2O_4 \rightarrow 2Li^+ + 2CO_2 \uparrow + 2e^-$$

$$LiOR + CO_2 \rightarrow LiOC_2R$$

$$4Li + 3CO_2 \rightarrow Li_2CO_3 \downarrow + C$$

To better understand the decomposition process, C–V and differential electrochemical mass spectrometry (DEMS) tests were conducted on the LCO‖R-G battery. Fig. 5c presents the C–V curves for the first three cycles, where three oxidation peaks are observed in the first cycle, corresponding to the oxidation of $Li_2C_2O_4$. In the second cycle, these peaks significantly diminish, and by the third cycle, only one oxidation and one reduction peak remain, indicating that most $Li_2C_2O_4$ had decomposed. These results suggest that $Li_2C_2O_4$ undergoes substantial decomposition during the initial cycles.

Further confirmation of $Li_2C_2O_4$ decomposition is provided by DEMS analysis, as shown in Fig. 5d and e. The DEMS results for full cells with negative R-G as a comparison reveal fluctuations in gas evolution during battery cycling, particularly at voltages of 3.31 V and 3.91 V. These fluctuations align with the oxidation peaks observed in the C–V curves (Fig. 5c), confirming the decomposition of $Li_2C_2O_4$ within the voltage range of 3.31 V to 4.58 V. The detected CO_2 is a direct product of $Li_2C_2O_4$ decomposition, which is essential for the formation of the organic/inorganic SEI layer.

IR spectroscopy further supports the decomposition process. As shown in Fig. 5f, the characteristic peaks associated with $Li_2C_2O_4$ and C=O bonds disappeared after cycling, confirming the complete decomposition of $Li_2C_2O_4$. Additionally, the disappearance of the C–H peak in the C≡C bond region is attributed to lithium intercalation at the graphite edge, leading to the formation of lithium carbide compounds during cycling. The pre-lithiation of recycled graphite using lithium oxalate provides a dual benefit: it supplies lithium ions for SEI formation and generates CO_2, which contributes to the formation of a stable organic SEI layer. This process, which occurs within the voltage range of 3.31 V to 4.58 V, not only enhances the initial cycling performance of the battery but also improves its long-term stability. Therefore, the use of lithium oxalate in the regeneration of spent graphite is an effective and sustainable approach for enhancing lithium-ion battery performance, providing both immediate and lasting improvements to battery operation.

2.5 Economic and environmental assessment

Natural graphite is a valuable non-renewable resource, and the synthesis of artificial graphite demands substantial energy. Battery-grade graphite, characterized by higher technical specifications compared to ordinary graphite, necessitates comprehensive environmental and economic evaluations to determine the feasibility of industrial application of the experimental process. A comparative analysis was performed between the experimental process and established industrial processes, as illustrated in the roadmap of Fig. 6a. Route 1 entails direct disposal, incurring no production costs, energy consumption, or benefits, but poses severe and irreversible environmental risks due to residual electrolytes and lithium dendrites in waste graphite. Route 2 (this technology) involves the pretreatment of waste graphite to remove impurities, followed by concurrent lithium extraction and pre-lithiation processes, thereby optimizing the economic and environmental benefits of recycling waste graphite. Route 3 employs acid and base chemical reagents, specifically, 5 M H_2SO_4 and 35% w/w H_2O_2 solution for leaching. This method, while effective in impurity removal, results in substantial pollution and waste. Additionally, NaOH is used for sintering and purification at 500 °C. Route 4 involves high-temperature calcination, where waste graphite is calcined at 800–1200 °C and then graphitized above 2800 °C, leading to significant energy consumption.

Assuming the treatment of 1 ton of waste graphite, an environmental and economic assessment (EEA) was conducted across four routes, evaluating energy consumption, cost, environmental impact, and revenue. Detailed calculations are available in the ESI.† Route 1, which involves direct disposal, incurs no production costs or energy consumption but generates 1 ton of solid waste. As depicted in Fig. 6b, costs for the other routes can be roughly divided into power and reagent costs. The total costs for routes 2, 3, and 4 are \$1770.18, \$987.06, and \$2800.00 per ton, respectively. Environmental pollution data (Fig. 6c) reveal that route 1 mainly generates 1000 kg of solid waste pollution per ton. Route 2 primarily produces 500 kg per ton of recyclable waste liquid composed of ethanol and oxalic acid. Route 3 results in 33 013 kg per ton of wastewater, primarily acid, alkali, and heavy metal contaminants. Route 4 emits 124 kg per ton of harmful metal waste and exhaust gases. In terms of energy consumption (Fig. 6d), route 4 exhibits the highest usage at 56 000 kWh per ton, whereas routes 2 and 3 have lower consumption levels. The market price for waste LIB graphite ranges from \$150.70 to \$191.80 per ton, while battery-grade graphite is valued at \$3014.00 per ton. Upgrading waste graphite to battery-grade graphite not only optimizes resource utilization without pollution but also offers substantial economic gains. Revenue data (Fig. 6e) indicates that route 3 generates approximately \$3014.00 per ton. Route 2 recovers both graphite and lithium oxalate, with recovered lithium oxalate valued at \$245.22 per ton, totaling \$3259.22 per ton (referring to the latest market price of lithium oxalate at \$92 888 per ton). For route 4, a 10% waste factor results in an income of \$2712.60 per ton. To conclude, route 2, the technology proposed in this work, demonstrates superior economic benefits (\$3259.22 profit), minimal environmental impact (500 kg of liquid waste and 0 kg of solid waste) and reasonable energy consumption (1800 kWh). Its total cost (reagent + electric power cost

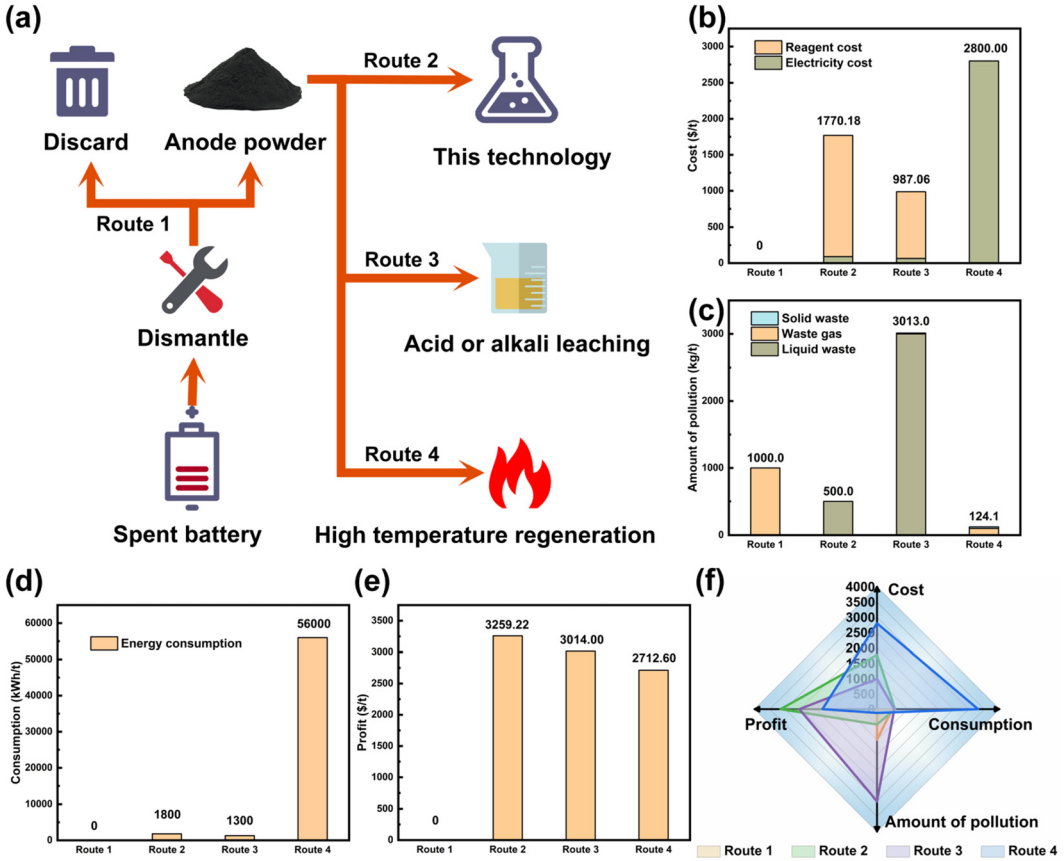

Fig. 6 (a) Schematic diagram of this experimental process and the three common industrial processes; (b) costs; (c) pollution status; (d) energy consumption; (e) benefits of the four different routes; and (f) comprehensive comparative radar plot of the four routes.

of \$1770.18) is more favorable compared to other methods, promoting a sustainable cycle of low cost, high efficiency, and minimal pollution (Fig. 6f).

3. Conclusion

In summary, this research introduces a novel and eco-friendly closed-loop regeneration technique for recycling non-renewable graphite anode materials from LIBs. Unlike traditional recycling methods that are energy-intensive and environmentally detrimental, the proposed process employs oxalic acid exclusively to effectively regenerate spent anodes, recover valuable metals, and synthesize pre-lithiation reagents. This approach provides a more sustainable and cost-effective solution. The study's key findings reveal that $Li_2C_2O_4$ formed on the surface of pre-lithiated regenerated graphite compensates for the loss of active Li^+ and acts as a sacrificial salt during battery operation. This oxalate decomposes during cycling, releasing CO_2 and mitigating adverse side reactions such as the formation of soluble lithium alkoxides and ester exchange in the electrolyte. Consequently, the regenerated graphite exhibits high electrochemical performance, with a specific capacity of 320.5 mAh g^{-1} after 200 cycles and a retention rate of 90.4%. Additionally, the method achieves an impressive Li^+ leaching rate of 97.64% under optimal conditions. From both environmental and economic perspectives, the method offers significant benefits, achieving a total economic return of \$3259.22 per ton of recycled graphite and minimal environmental impact. The low energy consumption and negligible waste generation position this method as a viable solution for large-scale graphite recycling in LIBs, thereby supporting resource sustainability and carbon reduction objectives. This study makes a substantial contribution to the field of material recycling, presenting a sustainable and economically beneficial alternative to conventional recycling practices. It provides a viable pathway for reducing the environmental footprint of spent LIBs and facilitates the shift towards a low-carbon economy.

4. Materials and methods

4.1 Materials and reagents

Retired lithium cobalt oxide (LCO) batteries were obtained from Apple cell phones and manually disassembled under a fume hood. The disassembled anode pieces were immersed in an ethanol solution for 30 minutes to remove the residual electrolyte. Since the binder used in the anode was aqueous

adhesive, the anode material and copper foil were separated by washing with deionized water. After removing most of the electrolyte and the binder, the washed and dried powder was collected and further dried in an oven at 80 °C for 12 hours to prepare it for subsequent processing. Anhydrous oxalic acid (AR, ≥99%) was purchased from Aladdin Reagent Co., Ltd.

4.2 Characterization methods

An Agilent ICP OES 720ES inductively coupled plasma emission spectrometer was utilized for the quantification of lithium in individual samples. A thermogravimetric analyzer (TGA) facilitated the assessment of optimal temperatures for impurity removal. Pretreatment was carried out in an OTF-1200X high-temperature tube furnace. The lithium concentrations were further quantified using a TAS-990 electronic absorption spectrophotometer. The physical phase characterization and crystal orientation of the powder samples were examined using a Bruker D8 ADVANCE X-ray diffractometer. Morphological characteristics were captured with a JEM-7800F field emission scanning electron microscope operating at 5.0 kV. Lattice structures of the samples were analyzed using a JEM-2100F field emission transmission electron microscope. Particle size distribution at various stages was evaluated using a BeNano 90 zeta potential particle sizer. Material composition and its variations were investigated with an IRTracer-100 infrared spectrometer. A JYH R800 Raman spectrometer was employed for further analysis. For the qualitative and quantitative assessment of gases emitted during battery operation, electrochemical mass spectrometry (ECMS) was implemented. Electrochemical performance testing was conducted using a CT2001A blue battery test system. Additionally, differential electrochemical mass spectrometry (DEMS) was utilized to monitor gas evolution during the battery's operational cycles.

4.3 Experimental component

Preparation of pretreatment graphite (P-G). The disassembled anode materials were annealed in a tube furnace under an air atmosphere at 550 °C for 2 h in order to ensure the complete elimination of the electrolyte, binder and other contaminants.

Preparation of regenerated graphite (R-G). 0.2 g of the pretreated P-G samples was mixed with varying amounts of anhydrous oxalic acid, and 40 mL deionized water was gradually added under continuous stirring at 200 rpm until oxalic acid was fully dissolved. This mixture was then transferred to an oil bath and heated to 130 °C with stirring at 200 rpm until complete evaporation occurred. The concentrated sample was subsequently oven-dried. Anhydrous ethanol was then added to the dried sample, followed by filtration. The filter residue was collected, rinsed multiple times with ethanol, and dried again in an oven. The final product was a lithium oxalate-enriched R-G anode, completing the pre-lithiation process.

4.4 Battery assembly

Half-cell fabrication. The anode was synthesized by blending the anode substance, conductive carbon and sodium alginate in an agate mortar at an 8 : 1 : 1 mass proportion and uniformly ground. The blend was then dissolved in deionized water to create a slurry, which was spread over a copper collector and dried at 80 °C for 12 hours. Lithium wafers served as the anode for the half-cells.

Full battery assembly. The cathode was prepared by integrating commercial lithium cobaltate ($LiCoO_2$), conductive carbon, and polyvinylidene fluoride (PVDF) in an onyx mortar in a 7 : 1.5 : 1.5 mass ratio. After uniform grinding, the composite was dissolved in *N*-methylpyrrolidone (NMP) to produce a slurry. The slurry was then spread onto an aluminum current collector and dried at 80 °C for 12 hours.

To maintain the N/P ratio of the cells between 1.03 and 1.5, assorted anode materials were combined with conductive carbon and sodium alginate at a 7 : 1.5 : 1.5 mass ratio, dissolved in deionized water to form a slurry, spread onto copper foil, and dried at 80 °C for 12 hours. The 2032 coin cells were conducted using 1 M $LiPF_6$ in a 1 : 1 v/v ethylene carbonate (EC) and diethylene carbonate (DEC) electrolyte, separated by a microporous tri-layer polypropylene (PP) separator. All battery-related tests were conducted under ambient temperature conditions.

4.5 Economic and environmental assessment

To perform the economic and environmental assessment (EEA) for the four proposed routes, we evaluated energy consumption, cost, environmental impact, and revenue. Power was assumed to cost $0.05 per kWh from clean energy sources. The market prices for oxalic acid and ethanol were $655.68 per ton and $737.64 per ton, respectively. Pollutant emissions were evaluated; processing each ton of graphite is estimated to discharge 500 kg of recyclable waste liquid composed of ethanol and oxalic acid.

Author contributions

Jie Chen: methodology, experimental design, data collection, experimental synthesis, investigation, and draft writing and editing. Ruilan Li: experimental synthesis, data analysis, and chart generation. Yongzhi Duan: experimental synthesis and data analysis. Shuaiqi Gong: manuscript revision, review & editing. Yulin Min: review & editing and investigation. Hexing Li: supervision and investigation. Penghui Shi: conceptualization, funding acquisition, project administration, and manuscript revision.

Conflicts of interest

The authors declare no competing financial interest.

Data availability

The data supporting this study's findings are available from the corresponding author upon reasonable request.

Acknowledgements

This work was supported by the National Natural Science Foundation of China (22406124) and the Science and Technology Innovation Plan of the Shanghai Science and Technology Commission (24ZR1425800).

References

1 P. Xu, D. H. S. Tan, B. Jiao, H. Gao, X. Yu and Z. Chen, *Adv. Funct. Mater.*, 2023, **33**, 2213168.
2 G. Harper, R. Sommerville, E. Kendrick, L. Driscoll, P. Slater, R. Stolkin, A. Walton, P. Christensen, O. Heidrich, S. Lambert, A. Abbott, K. Ryder, L. Gaines and P. Anderson, *Nature*, 2019, **575**, 75–86.
3 S. Natarajan and V. Aravindan, *Adv. Energy Mater.*, 2020, **10**, 2002238.
4 H. Tian, M. Graczyk-Zajac, A. Kessler, A. Weidenkaff and R. Riedel, *Adv. Mater.*, 2024, **36**, 2308494.
5 H. C. Kim, S. Lee and T. J. Wallington, *Environ. Sci. Technol.*, 2023, **57**, 11834–11842.
6 L. Zhang, Y. Zhang, Z. Xu and P. Zhu, *Environ. Sci. Technol.*, 2023, **57**, 13270–13291.
7 B. Moradi and G. G. Botte, *J. Appl. Electrochem.*, 2016, **46**, 123–148.
8 Y. Qiao, H. Zhao, Y. Shen, L. Li, Z. Rao, G. Shao and Y. Lei, *EcoMat*, 2023, **5**, e12321.
9 Y. Gao, J. Zhang, H. Jin, G. Liang, L. Ma, Y. Chen and C. Wang, *Carbon*, 2022, **189**, 493–502.
10 J. Kong, S. Zhou, T. He, S. Gu and J. Yu, *Green Chem.*, 2023, **25**, 3956–3965.
11 D. Yang, Y. Yang, H. Du, Y. Ji, M. Ma, Y. Pan, X. Qi, Q. Sun, K. Shi and L. Qie, *Green Energy Environ.*, 2024, **9**, 1027–1034.
12 Y. Li, W. Lv, H. Zhao, Y. Xie, D. Ruan and Z. Sun, *Green Chem.*, 2022, **24**, 9315–9328.
13 W. Ai, J. Jiang, J. Zhu, Z. Fan, Y. Wang, H. Zhang, W. Huang and T. Yu, *Adv. Energy Mater.*, 2015, **5**, 1500559.
14 J. Yu, M. Lin, Q. Tan and J. Li, *J. Hazard. Mater.*, 2021, **401**, 123715.
15 J. Zhang, Y. Lei, Z. Lin, P. Xie, H. Lu and J. Xu, *Chem. Eng. J.*, 2022, **436**, 135011.
16 Y. Guo, F. Li, H. Zhu, G. Li, J. Huang and W. He, *Waste Manage.*, 2016, **51**, 227–233.
17 J. Yang, E. Fan, J. Lin, F. Arshad, X. Zhang, H. Wang, F. Wu, R. Chen and L. Li, *ACS Appl. Energy Mater.*, 2021, **4**, 6261–6268.
18 K. Du, E. H. Ang, X. Wu and Y. Liu, *Energy Environ. Mater.*, 2022, **5**, 1012–1036.
19 R. Schmuch, R. Wagner, G. Hörpel, T. Placke and M. Winter, *Nat. Energy*, 2018, **3**, 267–278.
20 Z. Huang, Z. Deng, Y. Zhong, M. Xu, S. Li, X. Liu, Y. Zhou, K. Huang, Y. Shen and Y. Huang, *Carbon Energy*, 2022, **4**, 1107–1132.
21 C. Sun, X. Zhang, C. Li, K. Wang, X. Sun and Y. Ma, *Energy Storage Mater.*, 2020, **32**, 497–516.
22 C. Yang, H. Ma, R. Yuan, K. Wang, K. Liu, Y. Long, F. Xu, L. Li, H. Zhang, Y. Zhang, X. Li and H. Wu, *Nat. Energy*, 2023, **8**, 703–713.
23 Y. Sun, H.-W. Lee, Z. W. Seh, N. Liu, J. Sun, Y. Li and Y. Cui, *Nat. Energy*, 2016, **1**, 15008.
24 W. Ji, X. Zhang, M. Liu, T. Ding, H. Qu, D. Qiu, D. Zheng and D. Qu, *Energy Storage Mater.*, 2022, **53**, 613–620.
25 Q. Huang, M. Chen, Z. Huang, Y. Zhang, K. Ji and C. Wang, *J. Phys. Chem. C*, 2023, **127**, 4006–4014.
26 X. Li, X. Sun, X. Hu, F. Fan, S. Cai, C. Zheng and G. D. Stucky, *Nano Energy*, 2020, **77**, 105143.
27 K. Zou, W. Deng, P. Cai, X. Deng, B. Wang, C. Liu, J. Li, H. Hou, G. Zou and X. Ji, *Adv. Funct. Mater.*, 2021, **31**, 2005581.
28 L. Jin, C. Shen, A. Shellikeri, Q. Wu, J. Zheng, P. Andrei, J.-G. Zhang and J. P. Zheng, *Energy Environ. Sci.*, 2020, **13**, 2341–2362.
29 A. Veluchamy, C.-H. Doh, D.-H. Kim, J.-H. Lee, D.-J. Lee, K.-H. Ha, H.-M. Shin, B.-S. Jin, H.-S. Kim, S.-I. Moon and C.-W. Park, *J. Power Sources*, 2009, **188**, 574–577.
30 G. M. Overhoff, R. Nölle, V. Siozios, M. Winter and T. Placke, *Batteries Supercaps*, 2021, **4**, 1163–1174.
31 P. Bärmann, M. Mohrhardt, J. E. Frerichs, M. Helling, A. Kolesnikov, S. Klabunde, S. Nowak, M. R. Hansen, M. Winter and T. Placke, *Adv. Energy Mater.*, 2021, **11**, 2100925.
32 C. Yao, X. Li, Y. Deng, Y. Li, P. Yang, S. Zhang, J. Yuan and R. Wang, *Carbon*, 2020, **168**, 392–403.
33 M. Fan, Q. Meng, X. Chang, C. Gu, X. Meng, Y. Yin, H. Li, L. Wan and Y. Guo, *Adv. Energy Mater.*, 2022, **12**, 2103630.
34 G. Wang, F. Li, D. Liu, D. Zheng, Y. Luo, D. Qu, T. Ding and D. Qu, *ACS Appl. Mater. Interfaces*, 2019, **11**, 8699–8703.
35 G. Huang, J. Liang, X. Zhong, H. Liang, C. Cui, C. Zeng, S. Wang, M. Liao, Y. Shen, T. Zhai, Y. Ma and H. Li, *Nano Res.*, 2023, **16**, 3872–3878.
36 D. Shanmukaraj, S. Grugeon, S. Laruelle, G. Douglade, J.-M. Tarascon and M. Armand, *Electrochem. Commun.*, 2010, **12**, 1344–1347.
37 X. Zeng, J. Li and B. Shen, *J. Hazard. Mater.*, 2015, **295**, 112–118.
38 Y. Sun, J. Tang, K. Zhang, J. Yuan, J. Li, D.-M. Zhu, K. Ozawa and L.-C. Qin, *Nanoscale*, 2017, **9**, 2585–2595.
39 C. Yi, P. Ge, X. Wu, W. Sun and Y. Yang, *J. Energy Chem.*, 2022, **72**, 97–107.
40 E. G. Leggesse, C.-L. Chen and J.-C. Jiang, *Carbon*, 2016, **103**, 209–216.
41 Y. Gao, J. Zhang, Y. Chen and C. Wang, *Surf. Interfaces*, 2021, **24**, 101089.
42 R. Xiao, C. Kang, Y. Ren, J. Jian, B. Cui, G. Yin, Y. Ma, P. Zuo, G. Han and C. Du, *Chem. Commun.*, 2023, **59**, 13982–13985.
43 K. Tasaki, A. Goldberg, J.-J. Lian, M. Walker, A. Timmons and S. J. Harris, *J. Electrochem. Soc.*, 2009, **156**, A1019.

44 W. Zhong, S. Li, M. Liu, Q. Wu, Z. Zeng, S. Cheng and J. Xie, *Nano Energy*, 2023, **115**, 108757.
45 H. Du, Y. Wang, Y. Kang, Y. Zhao, Y. Tian, X. Wang, Y. Tan, Z. Liang, J. Wozny, T. Li, D. Ren, L. Wang, X. He, P. Xiao, E. Mao, N. Tavajohi, F. Kang and B. Li, *Adv. Mater.*, 2024, **36**, 2401482.
46 B. Strehle, S. Solchenbach, M. Metzger, K. U. Schwenke and H. A. Gasteiger, *J. Electrochem. Soc.*, 2017, **164**, A2513–A2526.
47 C.-J. Huang, Y.-C. Hsu, K. N. Shitaw, Y.-J. Siao, S.-H. Wu, C.-H. Wang, W.-N. Su and B. J. Hwang, *ACS Appl. Mater. Interfaces*, 2022, **14**, 26724–26732.